Faraday Discussions

Cite this: *Faraday Discuss.*, 2021, **230**, 30

PAPER

The role of surface oxidation and Fe–Ni synergy in Fe–Ni–S catalysts for CO_2 hydrogenation†‡

Claire E. Mitchell, [a] David Santos-Carballal, [b] Andrew M. Beale, [cd] Wilm Jones, [cd] David J. Morgan, [a] Meenakshisundaram Sankar *[a] and Nora H. de Leeuw *[abe]

Received 14th December 2020, Accepted 11th January 2021
DOI: 10.1039/d0fd00137f

Increasing carbon dioxide (CO_2) emissions, resulting in climate change, have driven the motivation to achieve the effective and sustainable conversion of CO_2 into useful chemicals and fuels. Taking inspiration from biological processes, synthetic iron–nickel-sulfides have been proposed as suitable catalysts for the hydrogenation of CO_2. In order to experimentally validate this hypothesis, here we report violarite $(Fe,Ni)_3S_4$ as a cheap and economically viable catalyst for the hydrogenation of CO_2 into formate under mild, alkaline conditions at 125 °C and 20 bar ($CO_2 : H_2 = 1 : 1$). Calcination of violarite at 200 °C resulted in excellent catalytic activity, far superior to that of Fe-only and Ni-only sulfides. We further report first principles simulations of the CO_2 conversion on the partially oxidised (001) and (111) surfaces of stoichiometric violarite ($FeNi_2S_4$) and polydymite (Ni_3S_4) to rationalise the experimentally observed trends. We have obtained the thermodynamic and kinetic profiles for the reaction of carbon dioxide (CO_2) and water (H_2O) on the catalyst surfaces *via* substitution and dissociation mechanisms. We report that the partially oxidised (111) surface of $FeNi_2S_4$ is the best catalyst in the series and that the dissociation mechanism is the most favourable. Our study reveals that the partial oxidation of the $FeNi_2S_4$ surface, as well as the synergy of the Fe and Ni ions, are important in the catalytic activity of the material for the effective hydrogenation of CO_2 to formate.

[a]*Cardiff Catalysis Institute, School of Chemistry, Cardiff University, Cardiff, CF10 3AT, UK. E-mail: Sankar@cardiff.ac.uk*

[b]*School of Chemistry, University of Leeds, Leeds, LS2 9JT, UK. E-mail: n.h.deleeuw@leeds.ac.uk*

[c]*Department of Chemistry, University College London, London, WC1H 0AJ, UK*

[d]*Research Complex at Harwell, Rutherford Appleton Laboratory, Harwell Science & Innovation Campus, Harwell, Didcot, OX11 0FA, UK*

[e]*Department of Earth Sciences, Utrecht University, Princetonlaan 8a, 3584 CB Utrecht, The Netherlands*

† Electronic supplementary information (ESI) available. See DOI: 10.1039/d0fd00137f

‡ All data obtained during this research are provided in full in the results section of this paper and data sets are openly available from the Cardiff University Research Portal at DOI: 10.17035/d.2020.0122176413.

Introduction

Although CO_2 acts as a pollutant, contributing to climate change and global warming, it can also be considered as a cheap and abundant C-1 building block for the production of simple carbon-based chemicals.[1,2] A barrier to this prospective beneficial use is the requirement to overcome the initial thermodynamically unfavourable CO_2 reduction step.[3] In contrast to synthetic catalysts,[4–6] nature has developed a sophisticated reaction pathway utilising mixed Fe–Ni clusters for efficient CO_2 reduction.[7] In prokaryotes, the core enzyme within the acetyl-CoA pathway, carbon monoxide dehydrogenase (CODH), is coupled with acetyl-CoA synthase (ACS). In a dual active site reaction, the reduction of CO_2 to CO is thought to occur with the help of electrons at the asymmetric [Ni–4Fe–5S] clusters.[8,9] The structures of these metal clusters within CODH–ACS are very similar to mineral forms of (Fe,Ni)S, leading to the intriguing theory that these minerals participated as catalysts in the early onset of life.[8–12] The electronic interaction between Fe and Ni has been well established to enhance catalytic performance.[13,14] The flexibility in coordination and charge transfer of Ni enables an important role in biological catalysis, which can also be relayed to chemical catalysis.[15] The synergy between Fe and Ni has been reported to lead to excellent catalytic performance for the reduction of CO_2 into methane[16] and CO,[17] and the reduction of HCO_3^- to formic acid;[18] the bimetallic materials outperform their analogous monometallic counterparts, which can be attributed to intermediate bond strengthening.[17,18] In 2019, Piontek *et al.*[11] synthesised and developed the pentlandite mineral, $Fe_{4.5}Ni_{4.5}S_8$, to mimic [NiFe] hydrogenase, which successfully performed in the electrocatalytic carbon dioxide reduction reaction (CO_2RR). Using aprotic solvents, CO_2RR was favoured over the hydrogen evolution reaction, with the main products of CO and methane. Despite the relatively unremarkable products, Piontek has shown the potential of these materials. The electrocatalytic abilities of the iron sulphide mineral greigite, Fe_3S_4, have also achieved success in the hydrogenation of CO_2,[19] albeit with low yields. Recently, we have reported the pyrrhotite material $Fe_{1-x}S$ as an effective catalyst for the hydrogenation of CO_2 *via* a HCO_3^- intermediate.[20,21] Calcination of the pyrrhotite catalyst increased the activity of the material, as a result of the formation of a unique O–Fe–S active site. The iron–nickel sulfide violarite, $(Fe,Ni)_3S_4$, is isostructural with greigite, and introducing Ni into this structure may therefore produce an even more successful catalyst as a result of the discussed enhanced electronic interaction. The Fe and Ni within violarite are distributed over tetrahedral and octahedral sites in a cubic close packed (ccp) array of S atoms.[22] Within the inverse thiospinel structure, half of the Ni cations occupy the tetrahedral sites, with the other Ni cations and the Fe atoms located in the octahedral positions.[23,24] The interaction of CO_2 with violarite has been compared to that with greigite (Fe_3S_4) in a computational study,[24] where replacing an Fe atom by Ni exhibited a strengthening effect on the binding of the CO_2 molecule, although not enough to activate it. Iron, nickel and sulphur are cheap, non-toxic, and readily available elements and catalysts made from them are therefore ideal for large-scale use, particularly if the reactions can occur under moderate reaction conditions.

In general, the low-Miller index surfaces are the most stable in spinel structured materials, expressed in both the computational[25] and experimental crystal

morphologies of natural[26] and synthetic samples.[27] The octahedral crystal habits of spinels are typically enclosed by (111) surfaces, where the corners may be truncated by (001) planes.[25,27] For example, the (001) and (111) surfaces have been prominent in high resolution transmission electron microscopy (HRTEM) images of polydymite (Ni_3S_4).[28,29] Moreover, density functional theory (DFT) simulations have also suggested that the low-Miller index planes of violarite ($FeNi_2S_4$) have the lowest surface energies.[30] The (001) and (111) facets of $FeNi_2S_4$ have been the subject of a number of studies, where their adsorption and catalytic properties towards H_2O[30] and CO_2 (ref. 31) have been assessed.

Building upon the foundation of previous work, here we report for the first time the facile synthesis, characterisation and catalytic application of violarite for the hydrogenation of CO_2. In tandem, we have employed DFT techniques to calculate the CO_2 conversion into formate in the presence of H_2O on the partially oxidised low-Miller index (001) and (111) surfaces of $FeNi_2S_4$ and Ni_3S_4. We have simulated the co-adsorption of the reactants on the partially oxidised sulfide surfaces, alongside the mechanistic pathways leading to the formation of formate, to examine their change of activity upon oxidation. Through investigation of the proposed synergy between Fe and Ni in the partially oxidised surfaces, violarite is revealed to be an excellent candidate to catalyse CO_2 hydrogenation into formate.

Materials and methods

Catalyst preparation

The (Fe,Ni)S synthesis was adapted[21] from the procedure reported by Beal *et al.*[32] using the following chemicals: iron(II) acetylacetonate $Fe(acac)_2$ (99.9%) (Molekula), nickel(II) acetylacetonate $Ni(acac)_2$ (Sigma Aldrich), sulfur (sublimed) (99.5%) (Alfa Aesar) and oleylamine (OAm) (70%) (Sigma Aldrich). The synthesis was carried out in a three-necked flask equipped with a condenser, temperature probe and magnetic stirrer bar. OAm was initially degassed by bubbling nitrogen rapidly for 30 minutes, and the synthesis was done under a nitrogen atmosphere. $Fe(acac)_2$ and/or $Ni(acac)_2$ (4.5 mmol, precursor molar ratios listed in Table 1) and sulfur (0.147 g, 4.5 mmol) were placed in a flask, and flushed with nitrogen. The degassed OAm (60 cm^3) was added and stirred to produce a dark red suspension. While constantly bubbling nitrogen through the reaction mixture, the suspension was rapidly heated to 310 °C and held for 12 hours before being cooled to room

Table 1 Samples 1–5, catalyst precursor ratios during synthesis and crystal structures of the materials, fresh and after 200 °C calcination. *Crystal structures determined from XRD spectra, Fig. S1

Sample number	$Fe(acac)_2$: $Ni(acac)_2$: sulfur (molar ratio)	Dominant structure(s)	
		Fresh	Calcined
1	1 : 0 : 1	$Fe_{1-x}S$	Amorphous
2	0.75 : 0.25 : 1	$Fe_{1-x}S/Ni_3S_2/(Fe,Ni)_3S_4$	$(Fe,Ni)_3S_4$
3	0.5 : 0.5 : 1	$(Fe,Ni)_3S_4$	$(Fe,Ni)_3S_4$
4	0.25 : 0.75 : 1	Ni_3S_2	$(Fe,Ni)_3S_4/NiS$*
5	0 : 1 : 1	Ni_3S_4/Ni_3S_2	Ni_3S_4*

temperature. To remove the OAm, acetone was added (40 cm^3), followed by centrifugation and the removal of the organic brown supernatant layer. To wash the black (Fe,Ni)S nanocrystals, the solid was then resuspended in toluene (Sigma Aldrich, 99.8%), followed by centrifugation. This step was repeated until the supernatant was clear and colourless. The sample was then left in a vacuum oven at room temperature overnight and stored as a powder in a sealed vial flushed with N_2.

Calcination of the powder was performed in a furnace with air flowing at a specific temperature, typically 200 °C, with a ramp rate of 5 °C min^{-1}, and the temperature was maintained for 4 hours. The material was then cooled to room temperature before being stored in a sealed vial flushed with N_2.

Catalytic CO_2 hydrogenation and product analyses

The hydrogenation of CO_2 to formate was carried out in a high-pressure stainless steel 10 mL autoclave reactor. In a typical reaction, 20 mg of the catalyst was charged in a glass liner containing 4 mL of 1 M NaOH and a stirrer bar; the glass liner was placed inside the autoclave reactor before the reactor was closed airtight. The reactor and its contents were first purged with N_2 (3 times) and then with CO_2 (3 times) to remove traces of air or oxygen from the system and then finally charged with 30 bar CO_2. The CO_2 was left to dissolve for 20 minutes at room temperature before the pressure was reduced to 10 bar, and then H_2 (10 bar) was added. Next, the reactor was heated to the reaction temperature (125 °C) while stirring at 1450 rpm. After 3 days of reaction, the reactor was cooled using an ice bath, the liquid sample was collected, and the solid catalyst was removed *via* centrifugation followed by filtration using a syringe filter fitted with a 45 μL filter tip. The identity of the product (HCOOH) was confirmed and quantified using proton nuclear magnetic resonance (^{1}H-NMR) analysis (Bruker 500 MHz spectrometer), where 0.7 mL of the reaction solution was mixed with 0.1 mL D_2O (for lock) and a sealed glass tube insert containing 1% tetramethylsilane (TMS) in $CDCl_3$ as an internal standard. A series of known standard solutions of formic acid were calibrated against the TMS insert, generating a calibration curve and response factors which were used for quantitative analyses of the reaction mixtures.

Catalyst characterisation

Powder X-ray diffraction. The bulk structures were characterised using X-ray diffraction. Conventional powder X-ray diffraction (PXRD) analysis of the materials was performed on a (θ–θ) PANalytical X'pert Pro powder diffractometer with a Ni filtered Cu Kα radiation source operating at 40 keV and 40 mA. Patterns were recorded over the 2θ angular range 10–80° using a step size of 0.016°.

***In situ* XRD.** *In situ* XRD experiments were performed on a Panalytical X'Pert diffractometer with an Anton Paar 900 K *in situ* cell. The XRD spectra were collected at temperatures between 25 °C and 800 °C under an air flow (10 mL min^{-1}). The sample was heated at a rate of 5 °C min^{-1} and was kept for 5 min at a certain temperature before the spectra were collected.

Raman spectroscopy. Raman spectroscopy was carried out with a Renishaw Ramascope, using a Spectrophysics 514 nm HeNe laser at a power of 10 mW. Spectra were obtained in the region of 100–1500 cm^{-1}.

Thermal gravimetric analysis. Thermal gravimetric analysis (TGA) was performed using a Setaram Labsys 1600 instrument. Samples (5–10 mg) were loaded into alumina crucibles and heated to 900 °C (5 °C min^{-1}) in a flow of synthetic air (50 mL min^{-1}). For all specified TGA runs, blank runs were subtracted from the relevant data to remove buoyancy effects.

X-ray photoelectron spectroscopy. X-ray photoelectron spectroscopy (XPS) was performed on a Thermo Fisher Scientific K-alpha$^+$ spectrometer. Samples were analysed using a micro-focused monochromatic Al X-ray source (6 mA × 12 kV; 72 W power) using the 400 μm spot mode of operation, which gives an elliptical analysis area of approximately 400 × 600 μm^2. Data were recorded at pass energies of 150 eV for survey scans and 40 eV for high resolution scans with 1 eV and 0.1 eV step sizes respectively. Charge neutralisation of the sample was achieved using a combination of both low energy electrons and argon ions. Data analysis was performed in CasaXPS using a Shirley type background and Scofield cross sections, with an energy dependence of −0.6.

X-ray absorption spectroscopy. X-ray absorption spectroscopy (XAFS) data were collected at the B18 beamline at the Diamond Light Source in Harwell, UK. The measurements were performed in transmission mode at the Fe and Ni K edge. A Si(111) double crystal monochromator was used to select the energies. A Pt coated mirror was used to reject higher harmonics from the beam. The photon flux of the incoming and outgoing X-ray beam was detected with two ionization chambers, I_0 and I_t, respectively, filled with appropriate mixtures of N_2/Ar. A third ionization chamber (I_{ref}) was used in series to simultaneously measure the corresponding metal foil reference. Data were processed using Athena software.

Computational details

The Vienna *Ab initio* Simulation Package (VASP) code was used to carry out spin-polarized simulations of all structures and energies within the usual Kohn–Sham implementation of density functional theory (DFT).[33–36] The *meta*-generalized gradient approximation (*meta*-GGA) was employed with the strongly constrained and appropriately normed (SCAN) semi-local density functional.[37] *Meta*-GGA functionals include the electron density as well as its first and second derivatives, the electron gradient and the non-interacting kinetic energy density terms, respectively, making them more accurate than their parent GGA approximations, which only have the first two types of contributions.[38–40] In particular, only the SCAN functional satisfies all 17 known exact constraints within the *meta*-GGA approach.[37] The inner electrons, comprising the levels [Ar] for Ni and Fe, [Ne] for S and [He] for O and C, the kinetic energy of the core states and the interaction with the valence states were described by the projector augmented wave (PAW) method,[41,42] whereas the electron of the H atom was treated as a valence electron. The non-spherical contributions to the gradient of the density were also included within the PAW spheres, which is essential for an appropriate simulation of the Ni and Fe d electrons when using *meta*-GGA functionals. Long-range dispersion interactions were applied using the D2 semi-empirical method of Grimme,[43] which is needed to describe properly the bulk and surface properties of different materials.[31,44–52] The Kohn–Sham valence states were expanded in a periodic plane-wave basis set with a cut-off fixed at 400 eV for the kinetic energy. The optimisation of the electronic density was considered converged when the energy

difference between two consecutive self-consistent loop steps was below 10^{-5} eV. We have used the Hubbard approximation[53] in the form of the scheme by Dudarev *et al.*[54] to improve the description of localized d states in the transition metal atoms. The values for the on-site Coulomb interaction term in this study were $U_{\text{eff}} = 1.7$ eV for Fe and 2.0 eV for Ni, which were developed by fitting the simulated lattice parameters of the pure greigite (Fe_3S_4) and Ni_3S_4 to their experimental values. The geometries were relaxed using an efficient conjugate-gradients technique based on the Newton line optimizer,[55,56] which was stopped when the Hellmann–Feynman forces on all atoms were smaller than 0.01 eV $Å^{-1}$. The saddle points and minimum energy paths (MEPs) between initial and final states were simulated using the climbing image nudged elastic band (cNEB) approach.[57,58] We used five images to model the MEP, which were optimised globally by means of the limited-memory Broyden–Fletcher–Goldfarb–Shanno (LBFGS) method.[55,59] The saddle points were characterised by single imaginary frequencies along the reaction coordinate, which were determined using the central finite differences method. These criteria allowed convergence of the total electronic energy to within 1 meV per atom.

The electronic integrations of the (001) and (111) surfaces of the thiospinels were calculated in reciprocal space using a Γ-centred Monkhorst–Pack (MP) sampling grid[60] containing $3 \times 3 \times 1$ k-points, which ensured a minimum spacing of 0.14 $Å^{-1}$ between k-points. However, the projection operators were evaluated in real space. The electronic partial occupancies were determined using the Gaussian smearing method with a smearing width of 0.05 eV. The tetrahedron method with Blöchl corrections[61] was used to obtain very accurate total energies. The isolated molecules were modelled in a cell with broken symmetry of $10.0 \times 10.5 \times 11.0$ $Å^3$, considering only the Γ point of the Brillouin zone.

The simulation cell of the thiospinel surfaces contained 56 atoms, distributed as 4 repeat formula unit (f.u.) layers stacked along the direction perpendicular to the surface. The two bottom-most repeat f.u. layers were kept frozen at their relaxed bulk positions, while the remaining layers were allowed to relax. A vacuum of 10 Å was added between the periodic images of the slab in the direction perpendicular to the surface. The ferrimagnetic configuration was considered for the thiospinels in our simulations, where the initial magnetic moments of the tetrahedral and octahedral sublattices were set antiparallel, with the ions in the high-spin state.[25,31,47,62–67] Dipole corrections perpendicular to the surface were applied in our simulations to account for any dipole created by the adsorbates.

The adsorption energies (E_{ads}) were defined as the difference between the energy of the surface slab containing the adsorbates and the sum of the energies of the isolated adsorbates and surface slab. The activation energy ($E_{\text{a}i}$) was calculated as the difference between the energy of the saddle point and the energy of the reactants, where the index i refers to each of the four elemental steps that we simulated. The energy of the elemental step (ΔE_i) was obtained as the difference between the energy of the products and the energy of the reactants.

Results and discussion

Catalytic testing and optimisation

(Fe,Ni)S catalysts were tested for the hydrogenation of CO_2 under hydrothermal conditions, using 1 M NaOH solvent, applying 20 bar pressure (at 25 °C

CO_2 : H_2, 1 : 1) before heating to a reaction temperature of 125 °C. Dissolution of CO_2 in alkaline aqueous media forms bicarbonate,[5] the desired intermediate for this reaction owing to the improved adsorption properties of HCO_3^- in comparison to CO_2.[18] To initiate this study, the catalyst synthesis procedure was first optimised. Iron nickel sulfide materials were synthesised by altering the $Fe(acac)_2$: $Ni(acac)_2$ precursor molar ratios, as presented in Table 1. All 5 samples were also calcined in flowing air at 200 °C to provide a series of 5 fresh and 5 calcined catalysts, which were tested for CO_2 hydrogenation. As presented in Fig. 1a, the freshly prepared $Fe_xNi_yS_z$ catalysts showed good performance for CO_2 hydrogenation in comparison to the monometallic iron and nickel sulfides. Sample 3, prepared with a 1 : 1 Fe : Ni precursor ratio, outperformed all other catalysts, producing 1.8 μmol of formate, in comparison to iron and nickel sulfides which produced 0.3 μmol and 1.2 μmol of formate, respectively. Calcining the samples improved the catalytic activity of all

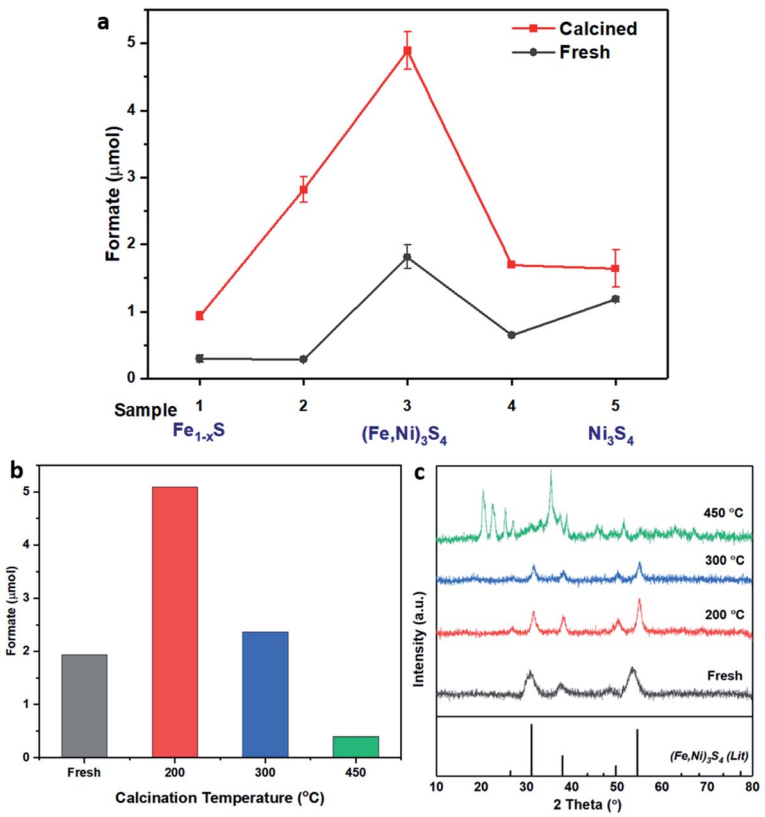

Fig. 1 (a) Catalyst comparison of fresh (black) and calcined (red) iron nickel sulfides with altering Fe : Ni ratio during synthesis. Sample preparation and labelling described in Table 1. Comparison of (b) formate productivity and (c) XRD of sample 3, $(Fe,Ni)_3S_4$: fresh (grey), calcined at 200 °C (red), 300 °C (blue) and 450 °C (green). Compared to violarite reference file (JCPDS 00-002-0779 PDF file). Reaction conditions: (Fe,Ni)S catalyst: 20 mg; 1 M NaOH solution: 4 mL; $p(CO_2)$: 10 bar (at 25 °C); $p(H_2)$: 10 bar (at 25 °C); reaction temperature: 125 °C; reaction time: 3 days.

samples, with sample 3 again providing the best catalytic performance, producing 4.9 μmol of formate.

The XRD pattern of the most active material, sample 3, presented in Fig. 1c, exhibits four major reflections, observed at 2θ values of approximately 31°, 38°, 50° and 55°, corresponding to the iron–nickel sulfide mineral violarite $(Ni,Fe)_3S_4$. The Fe-only sulfide, sample 1, corresponds to the pyrrhotite structure, $Fe_{1-x}S$, while the Ni-only sulfide, sample 5, predominantly consists of a polydymite (Ni_3S_4) structure; these structures are determined by the XRD diffraction patterns, presented in Fig. S1.† Samples 2 and 4 presented a mixture of $Fe_{1-x}S$, NiS, Ni_3S_2 and $(Fe,Ni)_3S_4$ structures, also observed in the XRD patterns. All XRD profiles are displayed and compared in Fig. S1.† A calcination pre-treatment at 200 °C enhanced violarite formation, observed as an increase in XRD peak intensity (Fig. 1c), and improved the catalytic activities for all 5 samples (Fig. 1a). This enhanced activity was previously discovered in pyrrhotite.[21] The results show that $Fe_{1-x}S$ and Ni_3S_4 have lower activity compared to $(Fe,Ni)_3S_4$, suggesting a synergy effect between Fe and Ni atoms. Increasing the calcination pre-treatment temperature to 300 °C and 450 °C lowers formate production to 2.4 and 0.4 μmol, respectively (see Fig. 1b). Calcination at 300 °C decreases the violarite crystallinity, as displayed in Fig. 1c, and at 450 °C iron and nickel sulfates and oxides begin to form, as discussed below. Commercial sources of Fe_3O_4, $NiSO_4$ and $FeSO_4$ were found to produce formate at a much lower quantity than all Fe_xNi_ySz samples synthesised here (see Table S1†), ruling out iron oxides or nickel sulfate as active species for CO_2 hydrogenation under these reaction conditions.

Calcination study and material characterisation

TGA and *in situ* XRD. Violarite is well known to oxidise spontaneously in air at room temperature and when heated.[68] To explore this behaviour, TGA and *in situ* XRD were performed on synthesised $(Fe,Ni)_3S_4$ with increasing temperatures under flowing air. Measuring the change in mass with increasing temperature using TGA (see Fig. 2a) and the change in the XRD reflections (phase) (see Fig. 2b) during calcination reveal a sequence of phase transformations, from the initial violarite structure at room temperature to fully oxidised nickel and iron oxide at 800 °C. The XRD patterns are depicted in more detail in Fig. 2c–e. The initial mass loss (up to ~150 °C) is the result of water and residual toluene evaporation from the surface. Between 25 and 200 °C, a steady increase in the crystallinity of $(Fe,Ni)_3S_4$ can be observed from the XRD, keeping the mass stable as observed by TGA. The structure then begins to lose its crystallinity and changes phase around 350 °C. Ascribing the small mass drop of 1% to evolution of SO_2, from 310 °C to 355 °C the substrate consists of a mixture of FeS_2, NiS_2 and $Fe_{1-x}S$, as well as remaining $(Fe,Ni)_3S_4$, together with the metal oxide species Fe_3O_4 and NiO, as shown in Fig. 2c. From 355 °C to 492 °C, there is a mass increase of 7.1%, as oxygen is incorporated into the structure, forming primarily the metal sulfates $FeSO_4$ and $NiSO_4$ (see Fig. 2d). As the temperature is increased from 620 °C, sulfate decomposition occurs, releasing SO_2 with a mass loss of 3.2%, which correlates with the final formation of the Fe_3O_4 and NiO crystal phases (as shown in Fig. 2e), and the increase in the iron oxidation state to iron(III). Allowing for subtle differences in temperature thresholds, these results are in good agreement with the outcomes reported by Dunn *et al.*[68]

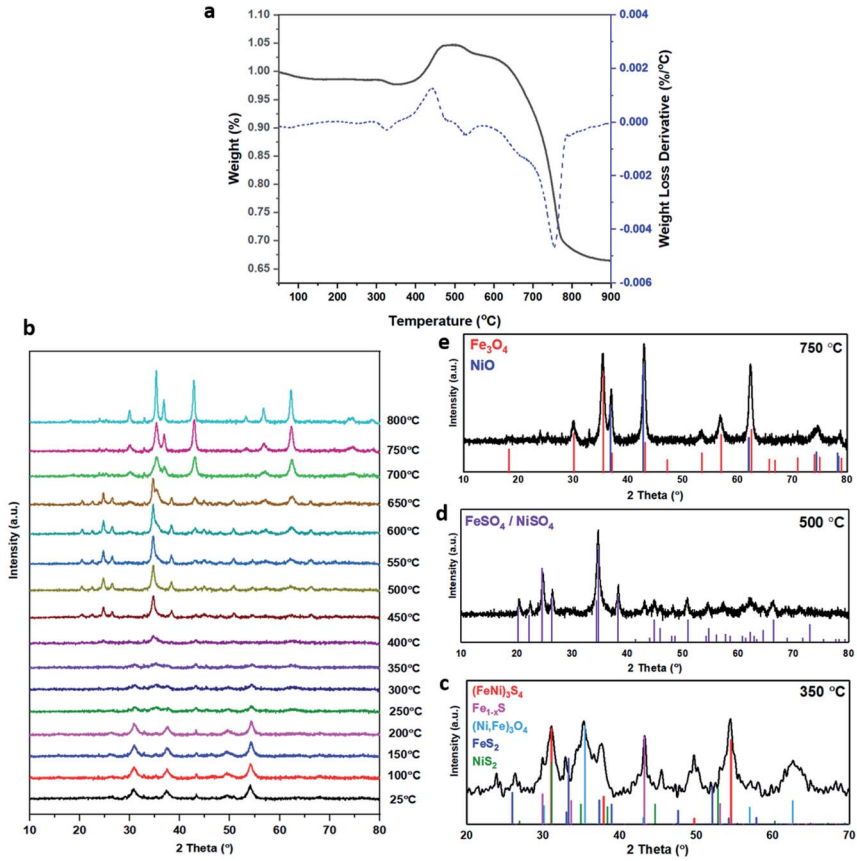

Fig. 2 (a) TGA of an $(Fe,Ni)_3S_4$ sample heated under air from room temperature to 800 °C at a heating rate of 5 °C min^{-1}. Percentage weight loss (black) and the first derivative of weight loss (blue). (b) *In situ* XRD patterns of the $(Fe,Ni)_3S_4$ sample, from 25 to 800 °C under flowing air at a heating rate of 5 °C min^{-1}. The XRD analysis was run every 50 °C. The peaks are analysed in more detail at specific temperatures: (c) violarite calcined at 350 °C, compared to the corresponding XRD patterns sourced from JCPDS files. Red – violarite, $(Fe,Ni)_3S_4$, 01-075-8684; dark blue – marcasite, FeS_2, 00-002-1342; green – vaesite, NiS_2, 01-071-4834; pink – pyrrhotite, $Fe_{1-x}S$, 01-079-5974; light blue – magnetite, Fe_3O_4, 01-074-1909/$(Ni,Fe)_3O_4$, 01-087-2336; (d) violarite calcined at 500 °C, compared to the corresponding XRD patterns sourced from JCPDS files. Purple – $FeSO_4/NiSO_4$, 00-013-0435; (e) violarite calcined at 750 °C, compared to the corresponding XRD patterns sourced from JCPDS files. Red – magnetite, Fe_3O_4, 01-074-1909; blue – nickel oxide, NiO, 01-078-437.

XPS analysis. XPS analysis was performed to determine the surface chemical composition and electronic structural change between the fresh and calcined $(Fe,Ni)_3S_4$ samples. The substantial range of iron, nickel and mixed Fe/Ni oxide/hydroxide compounds, and the complexity of their photoelectron spectra (including multiplet splitting and satellite features), makes any interpretation of unknown iron–nickel sulfide species very difficult,[69] and the XPS spectral interpretation must therefore be considered within context. XPS spectra for fresh and calcined $(Fe,Ni)_3S_4$ are presented in Fig. 3 with the binding energies, chemical

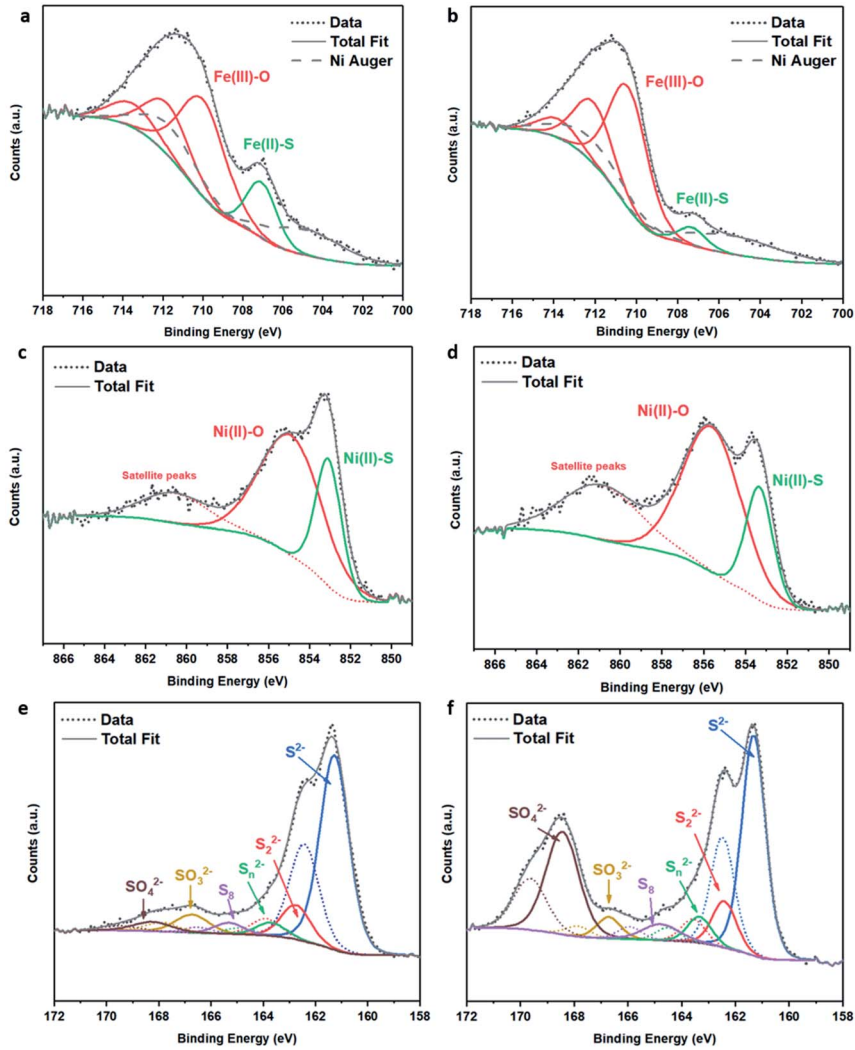

Fig. 3 XPS spectra of $(Fe,Ni)_3S_4$: (a) Fe 2p fresh, (b) Fe 2p calcined at 200 °C, (c) Ni 2p fresh, (d) Ni 2p calcined at 200 °C, (e) S 2p fresh, (f) S 2p calcined at 200 °C.

states and quantification listed in Table S2.† The spontaneous surface oxidation of metal sulfides when exposed to air or moisture is well known and results from the lower free energy of formation to form the metal oxides/hydroxides/sulfates.[69] The Fe 2p spectra (Fig. 3a and b) show the presence of the Ni $L_3M_{2,3}M_{4,5}$ Auger peaks at ~712–716 eV, in agreement with the Ni-rich nature of this mixed-metal material.[69] There are distinct Fe $2p_{3/2}$ peaks from 710 eV, indicating the presence of Fe(III)–O, and an Fe $2p_{3/2}$ peak at 707 eV corresponding to Fe(II)–S. Calcination of the sample enhanced the signal for the Fe(III)–O species, while that of the Fe(II)–S species is depleted. Note that no speciation of the Fe–O signal has been inferred through the fitting, but instead we represent the Fe–O species as a series of peaks taken from a bulk iron oxide. In the Ni 2p spectrum (Fig. 3c and d), the main

peaks at 853 eV and 855 eV correspond to the Ni(II)–S and Ni(II)–O Ni $2p_{3/2}$ peaks, respectively. In this instance, calcination causes only a marginal increase in the nickel oxide signal and a small decrease in the nickel sulfide signal in comparison to iron. The specific Ni(II)–S binding energy of 853.1 eV corresponds to Ni_3S_4/$(Fe,Ni)_3S_4$ coordination.[70] The Ni(II)–O Ni $2p_{3/2}$ peak for the fresh sample is observed at 854.9 eV, which McIntyre *et al.* ascribed to a composite of NiO and $NiFe_2O_3$.[71] Upon calcination, however, the Ni(II)–O peak exhibits a positive shift to 855.6 eV, corresponding to $NiFe_2O_4$, which implies that heating the surface in air causes enhanced Ni–Fe interaction.

The S 2p spectra are fitted with a doublet representing the spin–orbit splitting into S $2p_{3/2}$ and S $2p_{1/2}$ lines (Fig. 3e and f) and show the presence of many sulfur species, which we ascribe to monosulfide (161.3 eV), disulfide (162.6 eV), polysulfide (163.2 eV) and elemental sulfur (165.1 eV), together with sulfites SO_3^{2-} (166.8 eV) and sulfates SO_4^{2-} (168.5 eV). These binding energies are in excellent agreement with Buckley *et al.*[72] and Pratt *et al.*[73] Upon exposure to air, the migration of Fe and Ni towards the surface to combine with oxygen causes metal–sulfur bond cleavage and leaves metal vacancies within the structure, which forces the formation of S–S disulfide and polysulfide bonds. The formation of disulfides and polysulfides requires the oxidation of some sulfide (S^{2-}), which explains the presence of elemental sulfur,[73] as discussed in detail in our recent paper.[21] The S 2p XPS spectra reveal that the intensity of the Fe–S monosulfide peak at 161.3 eV significantly decreases, owing to the formation of SO_x species, which leaves Fe vacancies, thereby forcing the remaining Fe(II)–S to form disulfide bonds, as evident from Table S2.† The Fe 2p and Ni 2p spectra of fresh $(Ni,Fe)_3S_4$ can be compared to those of synthesised $Fe_{1-x}S$ and Ni_3S_4 samples (see Fig. S2 and Table S3†). The XPS spectra of $(Fe,Ni)_3S_4$ calcined at 300 °C (as shown in Fig. S3 and Table S4†) can be compared to those of the optimised sample calcined at 200 °C, providing further understanding of the active sites, and why increased thermal oxidation causes a drop in activity. The Fe 2p spectra (see Fig. S3a†) show a further drop in Fe(II)–S content, with the binding energy of Fe–S exhibiting a +0.8 eV shift in binding energy to 708.1 eV. In this range, Fe–S is becoming more oxidised, forming more Fe(III)–S character.[74] The Ni 2p spectrum loses Ni(II)–S character and exhibits new peaks at 855.6 eV and 858.8 eV, corresponding to the formation of $NiSO_4$, correlating with the work of Legrand.[75] The S 2p spectrum reveals a drop in monosulfide content and an increase in disulfide content as more metal–sulfide bonds are cleaved in favour of metal oxides. The evidence for Fe(III)–S and $NiSO_4$ shows that the enhanced interaction between Fe and Ni is lost. The atomic Fe : Ni : S : O ratios in fresh and calcined $(Fe,Ni)_3S_4$ samples were calculated as approximately 12 : 10 : 36 : 42 and 10 : 7 : 23 : 60, respectively, corresponding to a highly oxidised surface, although surface sulfur was still present after calcination. The crucial role of surface oxygen and sulfur is discussed in detail in the computational findings below.

XAFS and XANES analysis. The XAFS technique has rarely been systematically applied to iron nickel sulfide minerals,[76–78] and the present analysis therefore provides further understanding of these materials. The XAFS data for fresh $(Fe,Ni)_3S_4$, samples calcined at both 200 and 300 °C, the Fe–S reference ($Fe_{1-x}S$) and the Ni–S reference (Ni_3S_2) are displayed in Fig. 4. Turning our attention to the Fourier transform EXAFS, where the data are

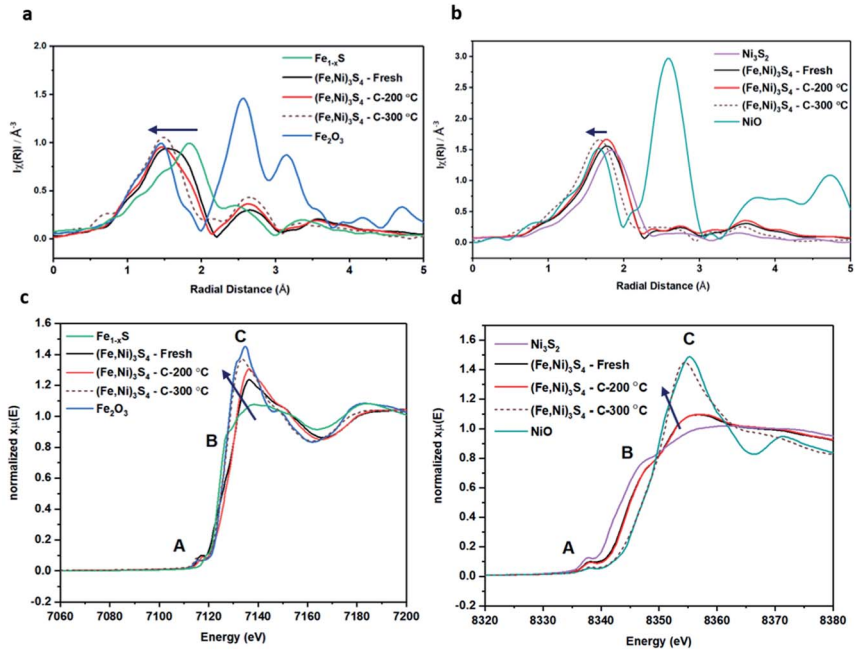

Fig. 4 XAFS data of violarite samples and reference samples: (a) FT-EXAFS Fe K-edge, (b) FT-EXAFS Ni K-edge. (c) XANES Fe K-edge, (d) XANES Ni K-edge. Fresh violarite (black), violarite calcined at 200 °C (red), violarite calcined at 300 °C (brown-dashed), $Fe_{1-x}S$ (green), Fe_2O_3 (blue), Ni_3S_2 (purple), NiO (teal). The blue arrow indicates the direction of increasing oxygen ligands.

phase-uncorrected, the Fe spectrum in Fig. 4a shows that fresh violarite has an Fe first shell radial distance of 1.55 Å, which is smaller than the equivalent Fe–S radial distance found in $Fe_{1-x}S$ represented by the peak situated at 1.8 Å, and larger than 1.45 Å for Fe–O in Fe_2O_3, thus revealing a mixture of Fe–S and Fe–O character within the violarite material, further implied by the broadness of the peak. The Fourier transform in Fig. 4b presents the average Ni scattering distances, where violarite is represented by a peak at 1.75 Å, *i.e.* a radial distance that is smaller than the 1.84 Å for Ni–S in Ni_3S_2. The average Ni–S bond distance in Ni_3S_4 is smaller than that in Ni_3S_2 (ref. 79) as a result of a mixture of tetrahedral and octahedral coordination, which causes shorter bond distances in comparison to fully octahedral coordination as seen in Ni_3S_2. Substituting Fe into the structure (Ni_3S_4 to $(FeNi)_3S_4$) decreases the average Ni–S bond distance even further when Fe substitutes into octahedral sites.[76] This is further evidence for violarite exhibiting an inverse-spinel structure, *i.e.* Fe is situated within an octahedral coordination environment, while Ni is hosted in a mixture of octahedral and tetrahedral coordination environments.[80] Upon calcination at 200 °C, the aforementioned Fe violarite peak exhibits a small negative shift and peak broadening, as Fe gains more oxygen ligands, which does not occur for Ni, as the radial distance is maintained, and the ligands remain stable at this temperature. Calcination at 300 °C causes a further negative shift in radial distance for both metals, as

more Fe–O and this time also Ni–O are formed. This loss of sulfide structure after calcination at 300 °C is reflected in the loss of crystallinity noted in the XRD spectra (see Fig. 1c), and in turn, a decrease in catalytic activity, as shown in Fig. 1b. It should be noted that low-spin Fe(II) and high-spin Fe(III) species with similar ligand systems can have similar bond distances, indicating that the radial distance of 1.55–1.65 Å may also be the result of low-spin Fe(II)–S and not high-spin Fe(III)–O, which is discussed in more detail later. The peaks at 2.6 Å in the FT-EXAFS Fe spectra for the violarite and Fe_2O_3 samples correlate to the Fe–Fe scattering component, indicating the presence of iron oxide in the sample, which is therefore possibly a mixture of Fe(III)–O and Fe(II)–S. However, XRD reveals the absence of iron oxide in the bulk sample. In the Ni spectra, the absence of a component at 2.6 Å shows that nickel oxides are not present in the bulk violarite samples, either fresh or calcined. Note that the TGA data (see Fig. 2a) revealed no SO_2 evolution at this calcination temperature, and thus sulfur still remains within the structure.

XANES analysis provides the opportunity to study the iron K-edge and nickel K-edge, presented in Fig. 4c and d, respectively. First to note is a characteristic pre-edge (feature A) from the contribution of the Fe/Ni 1s to Fe/Ni 3d transition.[65,81] There is a shoulder to the edge (B), indicating the coordination between Fe/Ni and S and representing the normally forbidden Fe/Ni 1s to Fe/Ni 4s transition. There is also white line intensity (C), corresponding to the first allowed Fe/Ni 1s to Fe/Ni 4p transition.[65,81] Fe/Ni oxide can be characterised by a sharp white line intensity (C), while Fe/Ni sulfide displays a broad XANES edge. Within the Fe XANES K-edge, there is an intense peak at feature C for the fresh violarite sample and the sample calcined at 200 °C, compared to $Fe_{1-x}S$, which confirms the presence of an Fe oxide-like character within the violarite material. The Ni XANES edge at region C is broad and without oxide character below 200 °C calcination temperature. Calcining the material at 300 °C causes an increase in intensity at C for both Fe and Ni, as Fe–S and Ni–S character is lost, forming Fe_3O_4, $FeSO_4$ and $NiSO_4$ structures, as indicated by XRD and illustrated in Fig. 2c. In the Ni XANES spectrum (see Fig. 4d), the shoulder at B indicates the coordination between Ni and S as seen for Ni_3S_2. Ni in Ni_3S_2 adopts tetrahedral coordination, exhibiting lower energy, while in NiO it adopts octahedral coordination, exhibiting higher energy. Violarite presents a shoulder at feature B, with higher energy than Ni_3S_2 and lower energy than NiO, indicating that Ni–S contributes mixed tetrahedral and octahedral sites. Feature A is also consistent with the expected tetrahedral/octahedral Ni environments of violarite, namely the feature is higher energy for tetrahedral Ni environments (Ni_3S_2) due to lack of inversion symmetry around the metal ion. Thus, at feature A violarite exhibits a lower energy than the Ni_3S_2 tetrahedral environment and a higher energy than the NiO octahedral environment due to its mixed Ni geometry. Calcination at 200 °C appears to have little effect on the coordination of nickel, but increasing the calcination temperature to 300 °C causes a shift to higher energy at feature B and lower energy at feature A, indicating dominant Ni–O character and octahedral coordination. The Fe XANES spectrum in Fig. 4c also reveals coordination information. Still focusing on shoulder edge B, violarite lies at a higher energy than $Fe_{1-x}S$ and Fe_2O_3. In $Fe_{1-x}S$ and Fe_2O_3, iron adopts Fe(III) high-spin state octahedral coordination, although tetrahedral Fe coordination would possess lower energy, while the higher energy of the iron in violarite is the result of octahedral coordination in the Fe(II) low-spin

state.[80] Upon calcination at 200 °C, Fe shifts only marginally to a higher energy at feature B as Fe replaces sulfur with oxygen ligands whilst maintaining the Fe(II) low-spin state, whereas calcination at 300 °C causes a large shift to lower energy, caused by the transformation into iron oxide, with the Fe(III) high-spin state and octahedral coordination. It may be deduced that Fe–O species are forming, while Ni remains stable as coordinated Ni–S within the bulk. Fe–O formation within iron sulfide structures has previously resulted in enhanced catalytic capabilities, which is discussed in detail in previous work.[21] We should remember that the metal oxidation states are $Fe^{2+}Ni_2{}^{3+}S_4$ in bulk violarite. Fe(III) has a high redox potential situated at +0.77 eV, and is thus easily reduced. Using supporting evidence from XPS and XAFS, we can conclude that Ni(III) in violarite is capable of maintaining Fe(II) in the lower oxidation state. This is vital for stabilising these important S–Fe–O active sites, resulting in improved catalytic activity compared to the pyrrhotite structure, where nickel is absent.[21]

Calculated reaction profiles

Our initial experimental findings, discussed above, have shown that surface-oxidised violarite is a superior catalyst for the hydrogenation of CO_2 compared to its Fe-only and Ni-only counterparts. We aim to aid the rationalisation of the catalytic trends observed in the experiments for our thiospinels through calculations based on density functional theory (DFT), where we apply and complement the knowledge gained from the materials characterisation. As such, we have studied the catalytic properties of the partially oxidised (001) and (111) surfaces of $FeNi_2S_4$ and Ni_3S_4 by simulating the co-adsorption and conversion of CO_2 and H_2O into formate and surface hydroxyls. We have decided to use the $FeNi_2S_4$ composition, which we identified in previous work to be dominant, with a very exothermic minimum, in the thermodynamic mixing between greigite and polydymite.[82]

We have used the most stable non-polar terminations to simulate the (001) and (111) surfaces, which were created from the bulk $FeNi_2S_4$ (ref. 83) and Ni_3S_4 (ref. 83) thiospinels using METADISE.[84] The most stable terminations of both the (001) and (111) facets were reconstructed Tasker type 3 surfaces, where half of the cations were shifted from the exposed layer of the relaxed side to the unrelaxed side of the slab to remove the unrealistic dipole perpendicular to the surface.[85] The simulations of the (001) surfaces were performed using a slab terminated in the bulk plane, comprising S atoms and octahedral cations and decorated by 0.5 monolayer (ML) of tetrahedral ions arranged in $(\sqrt{2} \times \sqrt{2})R45^\circ$ symmetry. The calculations of the (111) surface were carried out using a cell terminated by the face-centred cubic (fcc) close-packed plane of S atoms, decorated by 0.5 ML of both tetrahedral and octahedral ions, forming an incomplete hexagonal honeycomb arrangement. The partially oxidised surfaces were obtained by replacing 75% of the S atoms by O in the topmost layer of the surfaces, in as close agreement as possible with the XPS findings. We tested different scenarios and found that the substitution of the most coordinated S atoms led to the ground state configurations of the partially oxidised slabs, which are defined as *o*-$FeNi_2S_4$ and *o*-Ni_3S_4.

The reduction of CO_2 by H_2 to produce $HCOO^-$ under alkaline conditions takes place according to the equation:

$$CO_2(g) + H_2(g) + OH^-(aq) = HCOO^-(aq) + H_2O(l). \quad (1)$$

In order to simplify the computational simulation of eqn (1), we have considered that CO_2, once dissolved, reacts with $OH^-(aq)$, producing bicarbonate $[HCO_3^-(aq)]$ as

$$CO_2(g) + OH^-(aq) = HCO_3^-(aq). \quad (2)$$

We have also assumed that H_2 adsorbs dissociatively on the spinel sulfides, as we have seen this behaviour on greigite:[86]

$$H_2(g) = 2H^*, \quad (3)$$

where * indicates the adsorbed species.

The combination of eqn (1)–(3) leads to the simplified chemical reaction simulated in this work for the conversion of CO_2 into $HCOO^-$:

$$CO_2(g) + H_2O(g) = HCO_3^* + H^* = HCOO^* + OH^*. \quad (4)$$

Note that we have not represented the solubility of gaseous CO_2 and H_2 in water or the vapour pressure of H_2O in equilibrium with its condensed phase, as these processes occur in the liquid phase before any interaction of these species with the surface of the catalysts. The gaseous species are treated as isolated molecules in our calculations.

We have intentionally not considered the desorption of the final products HCOO* and OH*, since that would entail modelling isolated charged species. In the context of our simulations, the surface supercell of the Fe–Ni sulfides is wide enough to act as a source or sink of electrons, ensuring that the final adsorbed products are negatively charged, similar to the way that spin-forbidden reactions are allowed in heterogeneous catalysis.[87,88]

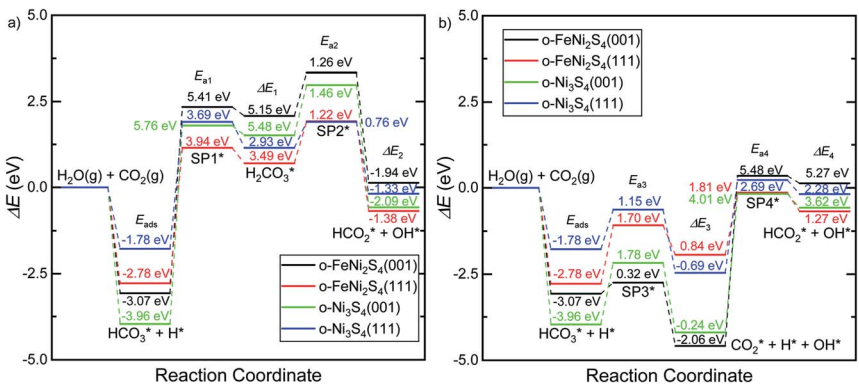

Fig. 5 Minimum energy pathways for CO_2 reduction by H_2O *via* (a) substitution and (b) dissociation mechanisms on the (001) and (111) surfaces of the *o*-$FeNi_2S_4$ and *o*-Ni_3S_4 thiospinels. Minimum states and saddle points are denoted by horizontal lines linked by dashed lines. Energies are referenced to the isolated H_2O and CO_2 molecules as well as the surface slab. Adsorbed species are denoted using the symbol *. Adsorption energies (E_{ads}), elemental step energies (ΔE_i) and activation energies (E_{ai}) are also indicated.

Fig. 5 displays the minimum energy pathways (MEPs) for CO_2 reduction by H_2O on the (001) and (111) surfaces of the *o*-$FeNi_2S_4$ and *o*-Ni_3S_4 thiospinels. We first modelled the co-adsorption of CO_2 and H_2O, which provides the elements needed to produce HCOO*. The co-adsorption of the reactants as HCO_3^* and H* on the (001) surfaces of *o*-$FeNi_2S_4$ and *o*-Ni_3S_4 releases the largest binding energy $E_{ads} = -3.07$ and -3.96 eV, respectively, which could lead to catalyst poisoning. Our calculations suggest that the least exothermic co-adsorption process takes place on the *o*-Ni_3S_4(111) surface, which is 1 eV less favourable than co-adsorption on the same facet of the *o*-$FeNi_2S_4$ counterpart. For CO_2 reduction into HCOO* on the thiospinel surfaces, we have proposed two alternative pathways *via* (i) substitution and (ii) dissociation mechanisms, shown in Fig. 5a and b, respectively, and in line with previous reports.[89,90] Elemental step 1 of the substitution mechanism leads to the formation of the $H_2CO_3^*$ intermediate, which is an endothermic process on any catalyst surface. Our calculations indicate that the most favourable elemental step 1 is promoted by the *o*-Ni_3S_4(111) surface, requiring 2.93 eV of energy, but the $H_2CO_3^*$ intermediate is still approximately 0.5 eV less stable than on the *o*-$FeNi_2S_4$(111) surface. The formation of the adduct $H_2CO_3^*$ on the *o*-Ni_3S_4(111) and *o*-$FeNi_2S_4$(111) surfaces has to overcome relatively large energy barriers $E_{a1} = 3.69$ and 3.94 eV, respectively. However, the activation energies and energy differences for elemental step 1 are more than 5 eV for the (001) surfaces of the two thiospinels, suggesting that these facets are not catalytically active for this process. Elemental step 2, where the adduct dissociates into HCO_2^* and OH*, is exothermic over all catalysts, releasing the largest energies on the two (001) surfaces. However, the *o*-$FeNi_2S_4$(001) surface also leads to products that are less stable than the initial isolated molecules and surface slab, further indicating the unsuitability of this catalytic system. The most stable final products were formed on the *o*-Ni_3S_4(001) and *o*-$FeNi_2S_4$(111) surfaces, while the most stable saddle points were calculated for the two (111) facets, which lie very close in our energy diagrams. Interestingly, activation energy 2 is ~0.5 eV lower on the *o*-Ni_3S_4(111) surface than on the *o*-$FeNi_2S_4$(111) surface, while the energy difference for elemental step 2 is ~0.70 eV lower for the *o*-Ni_3S_4(001) facet than for the *o*-$FeNi_2S_4$(111) facet.

Elemental step 3 of the dissociation mechanism is exothermic on all surfaces, apart from the *o*-$FeNi_2S_4$(111) surface where it requires $\Delta E_3 = 0.84$ eV (see Fig. 5b). However, the dissociation products CO_2^*, H* and OH* as well as saddle point 3 are more stable than the isolated CO_2, H_2O and surface slab, especially on the (001) facets. All the activation energies for elemental step 3 are below 1.80 eV, suggesting that they are feasible under our experimental conditions. Elemental step 4, where the H* atom attacks the activated CO_2^* molecule, is an endothermic reaction. We obtained the lowest energy of $\Delta E_4 = 1.27$ eV for elemental step 4 on the *o*-$FeNi_2S_4$(111) surface, with the remaining systems requiring more than 2.2 eV. The activation energies of saddle point 4 show a similar trend to the energies of elemental step 4, supporting the good catalytic performance of the *o*-$FeNi_2S_4$(111) surface.

In summary, our simulations show that the reaction of CO_2 with H_2O is thermodynamically spontaneous on the two surfaces of *o*-Ni_3S_4 and on the *o*-$FeNi_2S_4$(111) surface. The energy diagram of the substitution pathway also shows that all intermediates and transition states lie above the isolated H_2O and CO_2 molecules and surface slab, which are defined as the energy reference in our

study. The least unstable intermediates and saddle points of the substitution mechanism are found on the *o*-$FeNi_2S_4$ and *o*-Ni_3S_4(111) surfaces. However, for the dissociation mechanism, all intermediates and saddle points on the *o*-$FeNi_2S_4$(111) and *o*-Ni_3S_4(001) surfaces are more stable than the initial isolated reactants. The lowest activation energies for the dissociation pathway were calculated for the *o*-$FeNi_2S_4$(111) surface. Thus, according to both thermodynamic and kinetic arguments, the best catalytic activity is achieved on the *o*-$FeNi_2S_4$(111) surface for CO_2 reduction *via* a dissociation mechanism. Irrespective of their oxidation state, our results allow us to generalise that spinel-structured sulfides are catalytically active for the conversion of CO_2 *via* dissociation of the HCO_3^* surface species.[89]

To gain further insight into the mechanisms, we now analyse the geometries of the reactants and intermediates adsorbed on the most catalytically active *o*-$FeNi_2S_4$(111) surface. Fig. 6a shows that HCO_3^* exhibits bidentate coordination to the surface Fe and Ni atoms, at 1.93 and 1.98 Å, respectively, while an H atom sits on a nearby S atom at a distance of 1.34 Å. Following the formation of the $H_2CO_3^*$ intermediate, the Fe–O and Ni–O distances become shorter and are very similar, with an average value of 1.82 Å (see Fig. 6b). We found that the CO_2^* intermediate in the alternative dissociation mechanism remains in an activated configuration, since the bent apex angle is 125°, as shown in Fig. 6c. The larger stability of the CO_2^* intermediate with respect to $H_2CO_3^*$ can be rationalised in terms of its carbonate-like geometry, since it forms an additional bond to the surface O lying between the coordinated Fe and Ni atoms. Finally, the HCO_2^* product exhibits

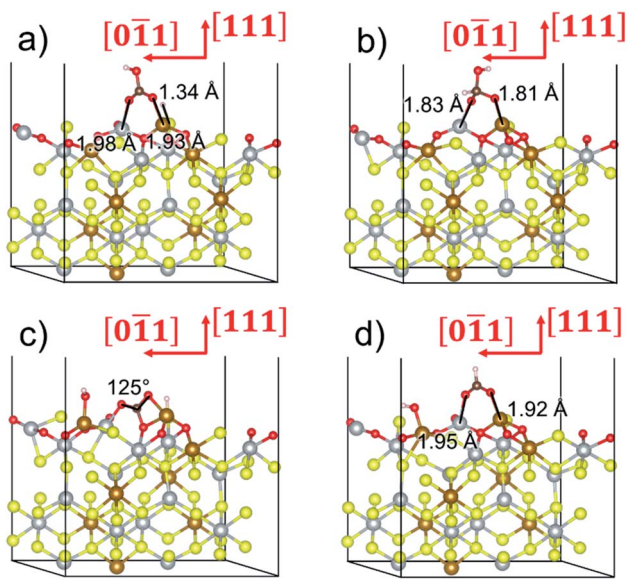

Fig. 6 Adsorption configurations of (a) reactants HCO_3^* and H*, (b) adduct $H_2CO_3^*$, (c) bent CO_2^* molecule, H* and OH* and (d) final products HCO_2^* and OH* on the *o*-$FeNi_2S_4$ (111) surface. Ni atoms are shown in grey, Fe atoms are shown in brown, S atoms are shown in yellow, O atoms are shown in red, C atoms are shown in dark brown and H atoms are shown in white.

a bidentate adsorption configuration similar to the one calculated for HCO_3^*, where the Fe–O and Ni–O bond distances become elongated to 1.92 and 1.95 Å, respectively (see Fig. 6d).

Conclusions

With the demand to produce a catalyst that is environmentally friendly, Earth-abundant, highly stable and produced *via* an economically viable synthesis, iron–nickel sulfides are promising candidates. In this work, violarite $(Fe,Ni)_3S_4$ has been synthesised within a shorter period of time (12 h) than any of the alternative methods reported in the literature.[91–93] Further investigation revealed that calcination at 200 °C favours violarite formation and improves the catalytic activity towards CO_2 hydrogenation. CO_2 and H_2 conversion into formate was achieved in alkaline media under mild hydrothermal conditions of 20 bar (CO_2 : H_2) and 125 °C. Violarite achieved superior results compared to Fe-only and Ni-only sulfides, *i.e.* $Fe_{1-x}S$ and Ni_3S_4, which implies that an enhanced synergistic interaction between Fe and Ni resulted in improved catalytic efficacy. A calcination study using *in situ* XRD and TGA displayed the many metal sulfide/sulfate/oxide structures that are formed and transformed during calcination at up to 800 °C, ending with fully oxidised Fe_2O_3 and NiO structures. XPS showed that the freshly synthesised violarite material possessed enhanced Ni–Fe interaction and electron transfer, whereas calcination at 200 °C formed a dominant metal oxide/sulfoxide surface. XAFS helped in analysing the bulk structural characteristics and oxidative effects of nickel and iron within the structure. Violarite possesses an inverse spinel structure, where Fe fills the octahedral holes and Ni has mixed tetrahedral and octahedral coordination, with little change in coordination and oxidation state observed upon calcination at 200 °C. FT-EXAFS of the Fe k-edge shows that iron possesses a mixture of Fe–O and Fe–S character and XANES reveals an Fe(II) low-spin octahedral state, suggesting O–Fe–S species. The enhanced crystallinity of partially oxidised violarite after calcination, as confirmed by XRD, indicates that the oxygen incorporated within the structure does not disrupt the crystal lattice. The bulk metal atoms have Fe(II) and Ni(III) oxidation states, where Ni(III) can facilitate charge transfer, which is essential to maintain the Fe(II) oxidation state.

We have also employed DFT+*U*-D2 calculations to investigate CO_2 conversion into formate on the partially oxidised low-Miller index (001) and (111) surfaces of $FeNi_2S_4$ and Ni_3S_4. We have simulated the co-adsorption of HCO_3^* and H* and found that these are thermodynamically feasible processes, leading to particularly stable configurations on both (001) surfaces, which could, however, poison the catalyst. The minimum energy pathway *via* the substitution mechanism involves unstable intermediates, while the saddle points have large activation energies. We identified that the carbonate-like intermediate is a key species, which means that the dissociation mechanism is the most likely to occur and that the partially oxidised $FeNi_2S_4$(111) surface is the most active catalyst. Experiments and computer simulations together have revealed that both the synergistic presence of Ni and Fe in the composition of the thiospinel violarite and the partial oxidation of its surface, expressed in the form of S–Fe–O moieties, are key for the enhanced catalytic performance of the material. Our work shows that violarite may play an

essential role in future CO_2 utilisation technologies for the production of sustainable fuels and chemicals.

Conflicts of interest

There are no conflicts to declare.

Acknowledgements

We acknowledge the Engineering and Physical Sciences Research Council (EPSRC grant EP/K009567) for funding. *Via* our membership of the UK's HEC Materials Chemistry Consortium, which is funded by EPSRC (EP/L000202, and EP/R029431), this work used the ARCHER UK National Supercomputing Service (http://www.archer.ac.uk). This research was undertaken using the Supercomputing Facilities at Cardiff University operated by the Advanced Research Computing @ Cardiff (ARCCA) Division on behalf of the Supercomputing Wales (SCW) project, which is part-funded by the European Regional Development Fund (ERDF) *via* the Welsh Government. Further work was undertaken on ARC4, part of the High-Performance Computing facilities at the University of Leeds, United Kingdom.

References

1 G. Centi, E. A. Quadrelli and S. Perathoner, *Energy Environ. Sci.*, 2013, **6**, 1711.
2 P. Styring, D. Jansen, H. de Coninck, H. Reith and K. Armstrong, *Carbon Capture and Utilisation in the green economy*, 2011.
3 A. Álvarez, M. Borges, J. J. Corral-Pérez, J. G. Olcina, L. Hu, D. Cornu, R. Huang, D. Stoian and A. Urakawa, *ChemPhysChem*, 2017, **18**, 3135–3141.
4 M. D. Porosoff, B. Yan and J. G. Chen, *Energy Environ. Sci.*, 2016, **9**, 62–73.
5 C. Mitchell, U. Terranova, I. AlShibane, D. J. Morgan, T. Davies, Q. He, J. Hargreaves, M. Sankar and N. H. De Leeuw, *New J. Chem.*, 2019, **43**, 13985–13997.
6 H. Yang, C. Zhang, P. Gao, H. Wang, X. Li, L. Zhong, W. Weiab and Y. Sun, *Catal. Sci. Technol.*, 2017, **7**, 4580–4598.
7 H. Dobbek, *Science*, 2001, **293**, 1281–1285.
8 M. J. Russell and W. Martin, *Trends Biochem. Sci.*, 2004, **29**, 358–363.
9 R. Vasiliadou, N. Dimov, N. Szita, S. F. Jordan and N. Lane, *Interface Focus*, 2019, **9**, 20190073.
10 A. Yamaguchi, M. Yamamoto, K. Takai, T. Ishii, K. Hashimoto and R. Nakamura, *Electrochim. Acta*, 2014, **141**, 311–318.
11 S. Piontek, K. junge Puring, D. Siegmund, M. Smialkowski, I. Sinev, D. Tetzlaff, B. Roldan Cuenya and U.-P. Apfel, *Chem. Sci.*, 2019, **10**, 1075–1081.
12 B. Konkena, K. junge Puring, I. Sinev, S. Piontek, O. Khavryuchenko, J. P. Dürholt, R. Schmid, H. Tüysüz, M. Muhler, W. Schuhmann and U.-P. Apfel, *Nat. Commun.*, 2016, **7**, 12269.
13 L. Wang, D. Li, M. Koike, S. Koso, Y. Nakagawa, Y. Xu and K. Tomishige, *Appl. Catal., A*, 2011, **392**, 248–255.
14 T. Zhang, Z. Liu, Y. A. Zhu, Z. Liu, Z. Sui, K. Zhu and X. Zhou, *Appl. Catal., B*, 2020, **264**, 118497.

15 J. Jiang, S. Lu, H. Gao, X. Zhang and H. Q. Yu, *Nano Energy*, 2016, **27**, 526–534.
16 D. Pandey and G. Deo, *J. Mol. Catal. A: Chem.*, 2014, **382**, 23–30.
17 L. R. Winter, E. Gomez, B. Yan, S. Yao and J. G. Chen, *Appl. Catal., B*, 2018, **224**, 442–450.
18 L. Gong, J. J. Chen and Y. Mu, *Phys. Chem. Chem. Phys.*, 2017, **19**, 28344–28353.
19 A. Roldan, N. Hollingsworth, A. Roffey, H.-U. Islam, J. B. M. Goodall, C. R. A. Catlow, J. A. Darr, W. Bras, G. Sankar, K. B. Holt, G. Hogarth and N. H. de Leeuw, *Chem. Commun.*, 2015, **51**, 7501–7504.
20 U. Terranova, C. Mitchell, M. Sankar, D. Morgan and N. H. De Leeuw, *J. Phys. Chem. C*, 2018, **122**, 12810–12818.
21 C. E. Mitchell, U. Terranova, A. M. Beale, W. Jones, D. J. Morgan, M. Sankar and N. H. de Leeuw, *Catal. Sci. Technol.*, 2021, **11**, 779–784.
22 D. J. Vaughan and J. R. Craig, *Am. Mineral.*, 1985, **70**, 1036–1043.
23 C. Tenailleau, B. Etschmann, R. M. Ibberson and A. Pring, *Am. Mineral.*, 2006, **91**, 1442–1447.
24 S. Posada-Pérez, D. Santos-Carballal, U. Terranova, A. Roldan, F. Illas and N. H. De Leeuw, *Phys. Chem. Chem. Phys.*, 2018, **20**, 20439–20446.
25 D. Santos-Carballal, A. Roldan, R. Grau-Crespo and N. H. de Leeuw, *Phys. Chem. Chem. Phys.*, 2014, **16**, 21082–21097.
26 D. Schüler, *J. Mol. Microbiol. Biotechnol.*, 1999, **1**, 79–86.
27 L. Zhao, H. Zhang, Y. Xing, S. Song, S. Yu, W. Shi, X. Guo, J. Yang, Y. Lei and F. Cao, *Chem. Mater.*, 2008, **20**, 198–204.
28 H. Wang, M. Liang, D. Duan, W. Shi, Y. Song and Z. Sun, *Chem. Eng. J.*, 2018, **350**, 523–533.
29 Q. Liu, A. Díaz, A. Prosvirin, Z. Luo and J. D. Batteas, *Nanoscale*, 2014, **6**, 8935–8942.
30 S. Haider, A. Roldan and N. H. De Leeuw, *J. Phys. Chem. C*, 2014, **118**, 1958–1967.
31 S. Posada-Pérez, D. Santos-Carballal, U. Terranova, A. Roldan, F. Illas and N. H. de Leeuw, *Phys. Chem. Chem. Phys.*, 2018, **20**, 20439–20446.
32 J. H. L. Beal, P. G. Etchegoin and R. D. Tilley, *J. Solid State Chem.*, 2012, **189**, 57–62.
33 G. Kresse and J. Hafner, *Phys. Rev. B: Condens. Matter Mater. Phys.*, 1993, **47**, 558–561.
34 G. Kresse and J. Hafner, *Phys. Rev. B: Condens. Matter Mater. Phys.*, 1994, **49**, 14251–14269.
35 G. Kresse and J. Furthmüller, *Phys. Rev. B: Condens. Matter Mater. Phys.*, 1996, **54**, 11169–11186.
36 G. Kresse and J. Furthmüller, *Comput. Mater. Sci.*, 1996, **6**, 15–50.
37 J. Sun, A. Ruzsinszky and J. Perdew, *Phys. Rev. Lett.*, 2015, **115**, 1–6.
38 D. Mejía-Rodríguez and S. B. Trickey, *Phys. Rev. B*, 2020, **102**, 1–4.
39 J. H. Yang, D. A. Kitchaev and G. Ceder, *Phys. Rev. B*, 2019, **100**, 1–10.
40 Y. Zhang, J. Sun, J. P. Perdew and X. Wu, *Phys. Rev. B*, 2017, **96**, 1–16.
41 P. E. Blöchl, *Phys. Rev. B: Condens. Matter Mater. Phys.*, 1994, **50**, 17953.
42 G. Kresse and D. Joubert, *Phys. Rev. B: Condens. Matter Mater. Phys.*, 1999, **59**, 1758–1775.
43 S. Grimme, *J. Comput. Chem.*, 2006, **27**, 1787–1799.
44 B. Farkaš, D. Santos-Carballal, A. Cadi-Essadek and N. H. de Leeuw, *Materialia*, 2019, **7**, 100381.

45 M. J. Ungerer, D. Santos-Carballal, A. Cadi-Essadek, C. G. C. E. van Sittert and N. H. de Leeuw, *J. Phys. Chem. C*, 2019, **123**, 27465–27476.
46 L. M. Botha, D. Santos-Carballal, U. Terranova, M. G. Quesne, M. J. Ungerer, C. G. C. E. van Sittert and N. H. de Leeuw, *RSC Adv.*, 2019, **9**, 16948–16954.
47 D. Santos-Carballal, P. E. Ngoepe and N. H. de Leeuw, *Phys. Rev. B*, 2018, **97**, 085126.
48 V. Postica, A. Vahl, J. Strobel, D. Santos-Carballal, O. Lupan, A. Cadi-Essadek, N. H. De Leeuw, F. Schütt, O. Polonskyi, T. Strunskus, M. Baum, L. Kienle, R. Adelung and F. Faupel, *J. Mater. Chem. A*, 2018, **6**, 23669–23682.
49 V. Postica, A. Vahl, D. Santos-Carballal, T. Dankwort, L. Kienle, M. Hoppe, A. Cadi-Essadek, N. H. de Leeuw, M.-I. Terasa, R. Adelung, F. Faupel and O. Lupan, *ACS Appl. Mater. Interfaces*, 2019, **11**, 31452–31466.
50 L. Reguera, N. L. López, J. Rodríguez-Hernández, M. González, C. E. Hernandez-Tamargo, D. Santos-Carballal, N. H. de Leeuw and E. Reguera, *Eur. J. Inorg. Chem.*, 2017, **2017**, 2980–2989.
51 B. Ramogayana, D. Santos-Carballal, P. A. Aparicio, M. G. Quesne, K. P. Maenetja, P. E. Ngoepe and N. H. de Leeuw, *Phys. Chem. Chem. Phys.*, 2020, **22**, 6763–6771.
52 A. Vahl, O. Lupan, D. Santos-Carballal, V. Postica, S. Hansen, H. Cavers, N. Wolff, M.-I. Terasa, M. Hoppe, A. Cadi-Essadek, T. Dankwort, L. Kienle, N. H. de Leeuw, R. Adelung and F. Faupel, *J. Mater. Chem. A*, 2020, **8**, 16246–16264.
53 V. I. I. Anisimov, M. A. A. Korotin, J. Zaanen and O. K. K. Andersen, *Phys. Rev. Lett.*, 1992, **68**, 345–348.
54 S. L. Dudarev, G. A. Botton, S. Y. Savrasov, C. J. Humphreys and A. P. Sutton, *Phys. Rev. B: Condens. Matter Mater. Phys.*, 1998, **57**, 1505–1509.
55 D. Sheppard, R. Terrell and G. Henkelman, *J. Chem. Phys.*, 2008, **128**, 134106.
56 M. R. Hestenes and E. Stiefel, *J. Res. Natl. Bur. Stand.*, 1952, **49**, 409.
57 G. Henkelman, B. P. Uberuaga and H. Jónsson, *J. Chem. Phys.*, 2000, **113**, 9901–9904.
58 G. Henkelman and H. Jónsson, *J. Chem. Phys.*, 2000, **113**, 9978–9985.
59 J. Nocedal, *Math. Comput.*, 1980, **35**, 773.
60 H. J. Monkhorst and J. D. Pack, *Phys. Rev. B: Solid State*, 1976, **13**, 5188–5192.
61 P. E. Blöchl, O. Jepsen and O. K. Andersen, *Phys. Rev. B: Condens. Matter Mater. Phys.*, 1994, **49**, 16223–16233.
62 A. Roldan, D. Santos-Carballal and N. H. de Leeuw, *J. Chem. Phys.*, 2013, **138**, 204712.
63 D. Santos-Carballal, A. Roldan, R. Grau-Crespo and N. H. de Leeuw, *Phys. Rev. B: Condens. Matter Mater. Phys.*, 2015, **91**, 195106.
64 D. Santos-Carballal, A. Roldan and N. H. de Leeuw, *J. Phys. Chem. C*, 2016, **120**, 8616–8629.
65 S. N. A. Zakaria, N. Hollingsworth, H. U. Islam, A. Roffey, D. Santos-Carballal, A. Roldan, W. Bras, G. Sankar, G. Hogarth, K. B. Holt and N. H. de Leeuw, *ACS Appl. Mater. Interfaces*, 2018, **10**, 32078–32085.
66 D. Santos-Carballal, A. Roldan, N. Y. Dzade and N. H. de Leeuw, *Philos. Trans. R. Soc., A*, 2018, **376**, 20170065.
67 D. Santos-Carballal, A. Roldan and N. H. De Leeuw, *Faraday Discuss.*, DOI: 10.1039/C9FD00141G.
68 J. G. Dunn and V. L. Howes, *Thermochim. Acta*, 1996, **282–283**, 305–316.

69 C. Zhao, C. Zhang, S. Bhoyate, P. K. Kahol, N. Kostoglou, C. Mitterer, S. Hinder, M. Baker, G. Constantinides, K. Polychronopoulou, C. Rebholz and R. K. Gupta, *Catalysts*, 2019, **9**, 597.
70 R. Karthikeyan, D. Thangaraju, N. Prakash and Y. Hayakawa, *CrystEngComm*, 2015, **17**, 5431–5439.
71 N. S. McIntyre, D. G. Zetaruk and D. Owen, *Appl. Surf. Sci.*, 1978, **2**, 55–73.
72 A. N. Buckley and R. Woods, *Appl. Surf. Sci.*, 1985, **20**, 472–480.
73 A. R. Pratt, I. J. Muir and H. W. Nesbitt, *Geochim. Cosmochim. Acta*, 1994, **58**, 827–841.
74 J. R. Mycroft, H. W. Nesbitt and A. R. Pratt, *Geochim. Cosmochim. Acta*, 1995, **59**, 721–733.
75 D. L. Legrand, H. Wayne Nesbitt and G. M. Bancroft, *Am. Mineral.*, 1998, **83**, 1256–1265.
76 J. Charnock, C. D. Garner, R. A. D. Pattrick and D. J. Vaughan, *Am. Mineral.*, 1990, **75**, 247–255.
77 R. T. Wilkin and D. G. Beak, *Chem. Geol.*, 2017, **462**, 15–29.
78 I. Bezverkhyy, P. Afanasiev and M. Danot, *J. Phys. Chem. B*, 2004, **108**, 7709–7715.
79 S. Liu, Y. Li, Y. Ju, J. Liu, J. Liu and Y. Shi, *Geochim. Cosmochim. Acta*, 2018, **222**, 1–16.
80 D. J. Vaughan, R. G. Burns and V. M. Burns, *Geochim. Cosmochim. Acta*, 1971, **35**, 365–381.
81 Y. Mikhlin, Y. Tomashevich, S. Vorobyev, S. Saikova, A. Romanchenko and R. Félix, *Appl. Surf. Sci.*, 2016, **387**, 796–804.
82 S. Haider, R. Grau-Crespo, A. J. Devey and N. H. de Leeuw, *Geochim. Cosmochim. Acta*, 2012, **88**, 275–282.
83 Y. Kesler, S. Smirnov, K. Pokholok and B. Viting, *Inorg. Mater.*, 1991, **27**, 977–980.
84 G. W. Watson, E. T. Kelsey, N. H. de Leeuw, D. J. Harris and S. C. Parker, *J. Chem. Soc., Faraday Trans.*, 1996, **92**, 433–438.
85 P. W. Tasker, *J. Phys. Chem. C*, 1979, **12**, 4977–4984.
86 A. Roldan and N. H. de Leeuw, *Phys. Chem. Chem. Phys.*, 2019, **21**, 2426–2433.
87 K. Reuter and M. Scheffler, *Phys. Rev. Lett.*, 2003, **90**, 4.
88 K. Reuter and M. Scheffler, *Phys. Rev. B: Condens. Matter Mater. Phys.*, 2003, **68**, 1–11.
89 A. Roldan, N. Hollingsworth, A. Roffey, H.-U. Islam, J. B. M. M. Goodall, C. R. A. A. Catlow, J. A. Darr, W. Bras, G. Sankar, K. B. Holt, G. Hogarth and N. H. De Leeuw, *Chem. Commun.*, 2015, **51**, 7501–7504.
90 C. S. He, L. Gong, J. Zhang, P. P. He and Y. Mu, *J. CO_2 Util.*, 2017, **19**, 157–164.
91 J. R. Craig, *Am. Mineral.*, 1971, **56**, 1303–1311.
92 F. Xia, J. Zhou, J. Brugger, Y. Ngothai, B. O'Neill, G. Chen and A. Pring, *Chem. Mater.*, 2008, **20**, 2809–2817.
93 W. H. Jørgensen, H. Toftlund and T. E. Warner, *Hydrometallurgy*, 2012, **115–116**, 98–103.